Tactile Super-Resolution Model for Soft Magnetic Skin

Youcan Yan, Yajing Shen, Chaoyang Song, and Jia Pan

***Abstract*—Tactile sensors of high spatial resolution can provide rich contact information in terms of accurate contact location and force magnitude for robots. However, achieving a high spatial resolution normally requires a high density of tactile sensing cells (or taxels), which will inevitably lead to crowded wire connections, more data acquisition time and probably crosstalk between taxels. An alternative approach to improve the spatial resolution without introducing a high density of taxels is employing super-resolution technology. Here, we propose a novel tactile super-resolution method based on a sinusoidally magnetized soft magnetic skin, by which we have achieved a 15-fold improvement of localization accuracy (from 6 mm to 0.4 mm) as well as the ability to measure the force magnitude. Different from the existing super-resolution methods that rely on overlapping signals of neighbouring taxels, our model only relies on the local information from a single 3-axis taxel and thereby can detect multipoint contact applied on neighboring taxels and work properly even when some of the neighbouring taxels near the contact position are damaged (or unavailable). With this property, our method would be robust to damage and could potentially benefit robotic applications that require multipoint contact detection.**

***Index Terms*—Force and tactile sensing, calibration and identification, perception for grasping and manipulation.**

I. Introduction

TACTILE sensing is essential for dexterous daily operation, spatial awareness and accurate contact localization for both humans and robots. To give robots the sense of touch, a variety of tactile sensors based on different principles have been developed recently, and comprehensive reviews can be found in [1]–[5]. Although great advancements in tactile sensing technology have been made, achieving high spatial resolution remains a big challenge for most tactile sensors.

For distributed tactile sensing arrays, each individual sensing cell is called a taxel, and the distance between the centers of two neighboring taxels defines the physical resolution of the sensor. To obtain a high spatial resolution, a high density of tactile sensing cells is generally required. However, a higher taxel density would inevitably lead to more wire connections and longer data acquisition time [6]. Moreover, as the sensing cell gets smaller, each taxel tends to be more sensitive to the external electromagnetic noises and the crosstalk between taxels gets amplified [1]. Due to such restrictions, the state-of-the-art distributed tactile sensing arrays only have a spatial resolution of $2.5\ \mathrm{mm}$ [7], which is still lower than that of human skin (up to $0.5\ \mathrm{mm}$ for SA1 afferents) [8]. Vision-based tactile sensors (e.g., GelSight [9] and GelSlim [10]) can achieve spatial resolution up to 1 μm (better than that of human skin), while they are relatively thick due to the layout requirements of the optical system. One alternative approach to improve the spatial resolution without increasing the density of the sensing cells is employing tactile super-resolution technology.

In general, tactile super-resolution leverages overlapping receptive fields of neighboring taxels to perceive stimulus details finer than the physical resolution of the sensor. This technique is analogous to the biological hyperacuity of human touch, by which tactile stimulus can be discriminated at a spatial resolution that is one order of magnitude higher than the average spacing between mechanoreceptors in the fingertip [11]. Thanks to the tactile hyperacuity, human hands can easily accomplish delicate operations like "blind" grasping and Braille reading. However, such super-resolution ability is still inferior in robotic skin.

In this letter, we propose a super-resolution model based on our previously developed soft magnetic skin [12], by which a 15-fold improvement of localization accuracy (from $6\ \mathrm{mm}$ to $0.4\ \mathrm{mm}$) was achieved. Different from [12] and the existing super-resolution methods that rely on overlapping signals of neighbouring taxels, our model only relies on the local information from a single 3-axis taxel by taking advantage of the self-decoupling property of Halbach magnets [13]. Therefore, it can detect multipoint contact applied on neighboring taxels and work properly even when some of the neighbouring taxels are damaged. Such property makes our method more robust to damage and could be beneficial to robotic applications that require multipoint contact detection.

II. Related Works

Recently, tactile super-resolution technology has drawn increasing attention among the robotics community, and a variety of super-resolution methods have been developed for different tactile sensors. [14] used Bayesian perception method to classify

Manuscript received September 7, 2021; accepted December 28, 2021. Date of publication January 10, 2022; date of current version January 28, 2022. This letter was recommended for publication by Associate Editor J. Falco and Editor D. Popa upon evaluation of the reviewers' comments. This work was supported in part by Hong Kong General Research Fund under Grants 11207818 and 11202119, and in part by the Centre for Transformative Garment Production. *(Corresponding author: Jia Pan.)*

Youcan Yan and Yajing Shen are with the Department of Biomedical Engineering, City University of Hong Kong, Hong Kong 999077, China (e-mail: ycyan4-c@my.cityu.edu.hk; yajishen@cityu.edu.hk).

Chaoyang Song is with the Department of Mechanical and Energy Engineering, Southern University of Science and Technology, Shenzhen 518055, China (e-mail: songcy@ieee.org).

Jia Pan is with the Department of Computer Science, University of Hong Kong, Hong Kong, China (e-mail: panjia1983@gmail.com).

Digital Object Identifier 10.1109/LRA.2022.3141449

contact location for a capacitive tactile sensor, by which a 35-fold improvement of the localization accuracy (from $4\,\mathrm{mm}$ to $0.12\,\mathrm{mm}$) was achieved. Using the same method, a 12- to 40-fold improvement of localization accuracy (from $4\,\mathrm{mm}$ to $0.1\,\mathrm{mm}$) was achieved for an optical tactile sensor (TacTip) in [15], [16]. [17] achieved a high contact localization accuracy ($1.1\,\mathrm{mm}$ in the best case) over a dome surface of approximately $1300\,\mathrm{mm}^2$ by using data-driven methods with only five barometric based Takktile pressure sensors, in which the localization accuracy was improved by around 15 times (from $15\,\mathrm{mm}$ to $1\,\mathrm{mm}$). Although significant improvement of the localization accuracy has been made, the above methods are still incomplete for tactile super-resolution, since the force magnitude is not measured simultaneously.

To tackle the above challenge, [18] designed a soft magnetic skin that can estimate both the contact position (XYZ coordinates) and force magnitude using neural networks, by which around 15-fold improvement of the localization accuracy was achieved (from $15\,\mathrm{mm}$ to $1\,\mathrm{mm}$). In [19], they employed multi-sensor learning combined with self-supervised loss to generalize their model to new sensor boards and skins, which makes it possible to replace the magnetic skin with no need to recalibrate the sensor. [20] used neural networks to determine the contact location for a multicurved robotic finger with sub-millimeter accuracy and achieved a force estimation error less than 10% of the true value. By employing machine learning, [21] achieved a localization accuracy of $5\,\mathrm{mm}$ and force estimation accuracy of $1.5\,\mathrm{N}$ (in the best case) on a sensing surface of $200 \times 120\,\mathrm{mm}$ by using only 10 strain-gauge sensors. More recently, [22] proposed a Local Message Passing Network (LoMP) for calibrating a piezoresistive sensor array, through which both the contact position and corresponding pressure map can be generated with a 16-fold super-resolved localization accuracy (from 5×5 to 20×20 grid). [23] introduced the concept of taxel value isolines (TVI) for estimating the contact position and force magnitude, and a 300-fold improvement of the localization accuracy was achieved (from $5\,\mathrm{mm}$ to $1/60\,\mathrm{mm}$) using neural networks. However, most of these methods would fail to work if one of the taxels near the contact position malfunctions due to some accidental factors (e.g., too large external forces), since the inputs of these neural networks rely on signals of not only the taxel being touched but also its neighbouring taxels.

To overcome this limitation, we propose a novel super-resolution method that can estimate both the contact position and force magnitude with a 15-fold improvement of the localization accuracy, and more importantly, it only relies on the readings of the taxel being touched, which ensures that the super-resolution model can work properly even when some of the taxels near the contact position are damaged (or unavailable). This is accomplished by designing a soft magnetic film. Different to the magnetic elastomer that is magnetized along the thickness direction [18], our magnetic film is magnetized in a sinusoidal manner as a flexible Halbach array. One benefit of such a magnetization manner is that the magnetic field under the film has two self-decoupled components in terms of the magnetic strength and the magnetic direction [12]. Taking advantage of this important property, the information of contact position can be properly decoupled with that of the force magnitude, and details of the super-resolution model can be found in Section IV.

III. Background

A. Sensor Design

As shown in Fig. 1(a), we design the tactile sensor as a sandwich structure, with a flexible magnetic film mixture of PDMS and NdFeB magnetic particles at a weight ratio of $1:3$) being the top layer (thickness $\sim 0.5\,\mathrm{mm}$ and $E \sim 2\,\mathrm{MPa}$), an elastomer sheet of PDMS being the middle layer (thickness $2.5\,\mathrm{mm}$) and magnetic sensors embedded on a printed circuit board being the bottom layer (thickness $1.6\,\mathrm{mm}$). When an external force is applied on the flexible magnetic film, the Hall sensor would sense the change of magnetic field due to the deformation of the film and the silicone elastomer.

Here, the flexible magnetic film is magnetized sinusoidally as a Halbach array [13], and thereby there are multiple north and south magnetic poles that are alternately arranged as shown in Fig. 1. Below the centers of the three north poles of the flexible magnet, there are three Hall sensors (S_1, S_2 and S_3) for measuring the magnetic flux densities. For ease of understanding, we can imagine each magnetic sensor as a virtual magnetic needle whose north pole always points to the direction of the magnetic field and the corresponding attraction force is always proportional to the magnitude of the magnetic field. If a normal force F_z (which is right above the sensor S_1 in Fig. 1(b)) is applied on the flexible magnet, the magnet will deform against the sensor S_1. Then the magnetic flux intensity B_{z1} along Z-axis will increase because the distance between the sensor S_1 and the flexible magnet reduces. This implies that the virtual magnetic needle will not rotate while the attraction force will increase.

Similarly, if an off-centered force F_z' is applied on the sensor (Fig. 1(b)), the deformation of the magnet would induce an increase of both B_{z2} and B_{z3} because the distance between the flexible magnet and the sensor S_2 and S_3 decreases. At the same time, there would be an opposite change on B_{x2} (< 0) and B_{x3} (> 0) since the north magnetic poles above S_2 and S_3 tilt in opposite directions, which leads to the virtual magnetic needles rotating in opposite directions as well. That is to say, based on the readings of three magnetic sensors (or the rotation of virtual magnetic needles), we can roughly locate the contact force to one side of a particular magnetic sensor. This rule applies to both a single 3-axis taxel and sensor arrays for single touch cases. For example, according to the above analysis, we can estimate that the contact position of F_z' is on the right side of S_2 (or on the left side of S_3). For multipoint contact detection, we can set an activation threshold of B_z readings for each taxel, and any number of taxels can be activated simultaneously.

To ensure that the tactile sensor can work properly, the polarity of magnetic poles located above each magnetic sensor should be the same (north pole here) and every two neighboring north poles should be separated by an opposite pole (south pole here). The period of the flexible magnet is $6\,\mathrm{mm}$, i.e., the distance between two neighboring magnetic poles is $3\,\mathrm{mm}$. Thus the distance between the centers of two neighboring magnetic sensors is set as $6\,\mathrm{mm}$ so that the above layout requirements can be satisfied. For

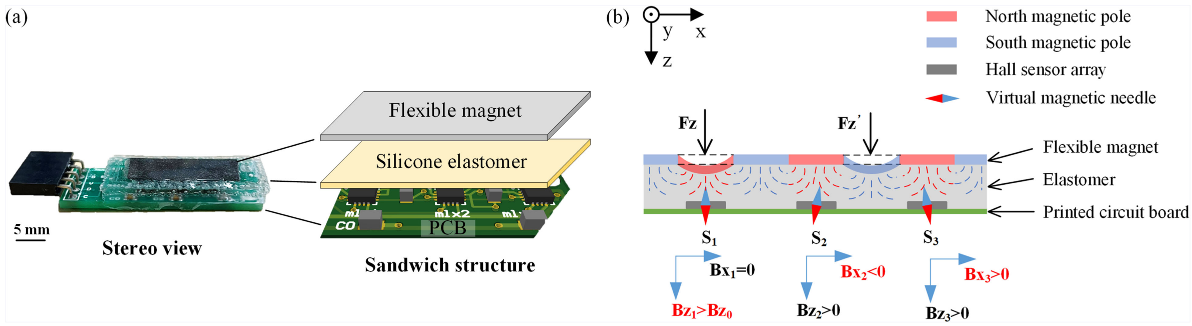

Fig. 1. (a) Structure of the tactile sensor. (b) Schematic illustration of the working principle.

more details of the sensor fabrication and applications, readers are referred to our previous work [12], [24], [25].

B. Halbach Array

The key component of the proposed tactile sensor is a sheet of flexible Halbach magnet, which has a continuous and quasi one-sided distribution of the magnetic field. Assume the flexible Halbach magnet has a planar structure which lies in the X-Y plane and has a thickness of d_0. The upper and lower surfaces of the planar structure are at $z = 0$ and $z = -d_0$, respectively. According to [13], the magnetic flux densities B_x (along X-axis) and B_z (along Z-axis) below the Halbach magnet can be derived as:

$$B_x = \mu_0 \frac{\partial \varphi_{\text{below}}}{\partial x} = -\mu_0 M_0 (1 - e^{kd_0}) e^{kz} \sin(kx) \quad (1)$$

$$B_z = \mu_0 \frac{\partial \varphi_{\text{below}}}{\partial z} = \mu_0 M_0 (1 - e^{kd_0}) e^{kz} \cos(kx) \quad (2)$$

where μ_0 is the permeability of free space and is equal to $4\pi \times 10^{-7}$ H/m, φ_{below} is the magnetostatic scalar potential below the flexible magnet, M_0 is the magnetization magnitude, and k is the wave number.

According to (1) and (2), we can calculate the overall (resultant) magnetic flux density $B(x, z)$ and the ratio $R_B(x, z)$ of B_x and B_z at any point (x, z) in the X-Z plane of a planar Halbach magnet as follows:

$$B(x, z) = \sqrt{B_x^2 + B_z^2} = \mu_0 M_0 (1 - e^{kd_0}) e^{kz} \quad (3)$$

$$R_B(x, z) = \tan \alpha(x, z) = \frac{B_x}{B_z} = \tan(kx), \quad (4)$$

where $R_B(x, z)$ or $\tan \alpha(x, z)$ indicates the magnetic direction relative to the Z-axis. From (3) and (4), we observe that the overall magnetic flux density $B(x, z)$ is independent of the x coordinate and the magnetic direction $\tan \alpha(x, z)$ is independent of the z coordinate, and thus $B(x, z)$ and $R_B(x, z)$ can be simply denoted as $B(z)$ and $R_B(x)$, respectively. By taking advantage of this self-decoupling property, the contact location and force magnitude can be simultaneously estimated just using a single 3-axis taxel. The following section explains the details of the proposed super-resolution method.

IV. Super-Resolution Model

Given the principle of the tactile sensor (Fig. 1(b)), we can roughly locate the contact force to the left ($B_x > 0$) or right

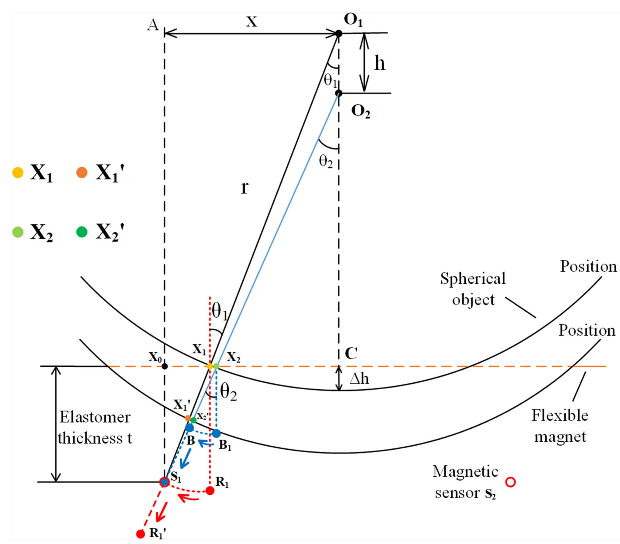

Fig. 2. Theoretical model of the proposed super-resolution method.

($B_x < 0$) side of the Hall sensor with the largest B_z among the three sensors. To further improve the localization accuracy, we developed a super-resolution model as shown in Fig. 2.

Here, we assume the radius of the spherical object is r, the contact position (i.e., the horizontal distance between the sphere center O_1 and the magnetic sensor S_1) is x, and the elastomer thickness (i.e., the vertical distance between the flexible magnet and Hall sensors) is t. Since the flexible magnetic film has a thickness of only 0.5 mm, which is roughly 3 times thinner than the elastomer layer (thickness 1.5 mm) of the sensor, the compression of the magnetic film would be much smaller than that of the elastomer layer when under external forces. Therefore, we made the following two assumptions for the model:

1) Ignore the compression of the flexible magnet (with 0.5 mm thickness) so that the magnetic properties of the film ((1) and (2)) are consistent during deformation.
2) Only consider the rotation and translation of the magnetic field when the flexible magnet is bent and moved, respectively.

Based on above assumptions, when the spherical object gradually approaches *Position* 1 where line S_1O_1 and the sphere outline intersect with the flexible magnet at X_1, the magnetic field at point R_1 (red solid circle) right below X_1 would gradually rotate to point S_1 (red hollow circle) as the flexible magnet

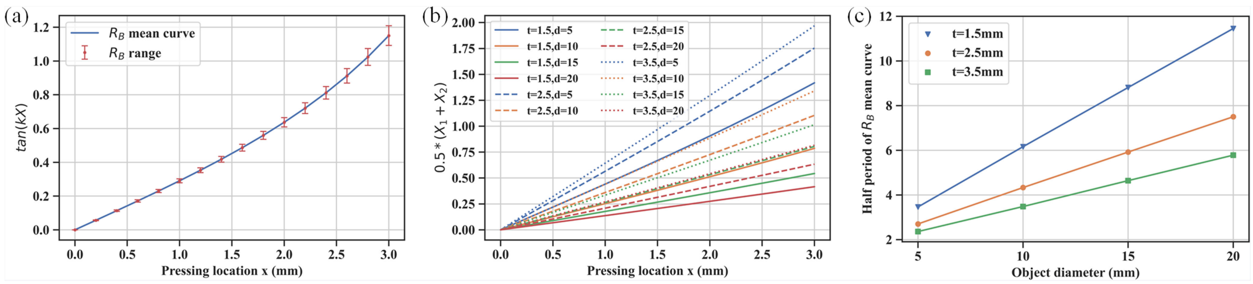

Fig. 3. Theoretical results of the super-resolution model. (a) R_B mean curve over the pressing location x. (b) Mean value of X_1 and X_2 over the pressing location x. (c) Trend of the half period $T/2$ under different indenter diameters and elastomer thicknesses.

bends. Further, when the sphere is pressed to $Position$ 2, the contact point X_1 will move along O_1X_1 to the point X_1' and the magnetic field at point R_1 will move from S_1 to R_1', and the length of segment X_1R_1 equals $X_1'R_1'$. We note that the actual position of X_1' should be along the direction of line O_2X_1, which is slightly on the left side of the current position of X_1' due to the expansion of the elastomer under pressure. Since the indentation depth h is much smaller than the sphere radius r, we assume that X_1' is still along O_1X_1.

Similarly, we perform reverse analysis to find out which point (fixed on the magnetic field) has shifted to S_1 when the sphere is pressed from the non-contact situation to $Position$ 2. Drawing a line from S_1 to O_2 (assume the intersection point between S_1O_2 and the flexible magnet is X_2), if the sphere is raising from $Position$ 2 to the non-contact situation, the magnetic field at point S_1 would first go back to point B along S_1O_2 when the sphere reaches $Position$ 1, and then rotate reversely back to B_1 which is right below the point X_2 when the sphere leaves the surface of sensor.

That is to say, when the sphere is pressed from $Position$ 1 to $Position$ 2, the magnetic sensor S_1 measures the magnetic flux density at points from R_1 to B_1, which corresponds to the horizontal location from X_1 to X_2. According to (4), the R_B value under the flexible magnet is only dependent of X coordinate. Since X_1 and X_2 are highly sensitive to the contact location x while insensitive to the change of force magnitude, we thereby define the R_B range $[R_B(X_1), R_B(X_2)]$ for estimating the contact location (see Fig. 3(a)), where $R_B(X_1)$ and $R_B(X_2)$ are minimum and maximum R_B values under an indentation depth from Δh to $\Delta h + h$ at contact location x, respectively. As a result, the minimum interval of pressing locations whose R_B ranges do not overlap between each other would be the best localization accuracy of the sensor.

To obtain the R_B range at contact position x, we need first calculate X_1 and X_2. Assume $\angle X_0S_1X_1$ and $\angle X_1O_1C$ are equal to θ_1, and $\angle X_0S_1X_2$ and $\angle X_2O_2C$ are equal to θ_2 (Fig. 2), in $\triangle X_0S_1X_1$ and $\triangle X_1O_1C$, we can calculate X_1 and $\sin(\theta_1)$ respectively as:

$$X_1 = t \cdot \tan(\theta_1), \ \ \sin(\theta_1) = (x - X_1)/r.$$

By eliminating the variable θ_1 using trigonometric identities, we can solve X_1 from the equation with $|X_1| \le |X_2|$:

$$X_1^4 - 2xX_1^3 + (x^2 + t^2 - r^2)X_1^2 - 2xt^2X_1 + x^2t^2 = 0. \tag{5}$$

Similarly, in $\triangle X_0S_1X_2$ and $\triangle X_2O_2C$, we can calculate X_2 and $\tan(\theta_2)$ respectively as:

$$X_2 = t \cdot \tan(\theta_2), \ \ \tan(\theta_2) = \frac{x - X_2}{r\cos(\theta_1) - h},$$

and we can solve X_2 as:

$$X_2 = \frac{xt}{\sqrt{r^2 - (x - X_1)^2} - h + t}. \tag{6}$$

At the same time, we can calculate Δh by deducting the length of O_1C from the radius r:

$$\Delta h = r - \sqrt{r^2 - (x - X_1)^2}. \tag{7}$$

Δh indicates the threshold of the indentation depth when the sphere outline and S_1O_1 intersect with the flexible magnet at the same point X_1.

Taking the elastomer thickness $t = 3.5\,\text{mm}$ and sphere diameter $d = 20\,\text{mm}$ as an example and let the indentation depth be $1\,\text{mm}$ (i.e., $\Delta h + h = 1$), we can calculate X_1 and X_2 according to (5) and (6), and we can also get the corresponding R_B range starting from $\tan(kX_1)$ to $\tan(kX_2)$ according to (4), which are as shown in Fig. 3(a). Note that in Fig. 3(a) the X in $\tan(kX)$ is in capital, indicating that the magnetic flux density at position X is sensed by the magnetic sensor S_1, and the R_B mean curve refers to the mean values of $R_B(X_1)$ and $R_B(X_2)$ over different contact location x. It is found that the R_B range increases as the contact location x increases, that is, the further the contact location is away from the center of the Hall sensor S_1 ($x = 0$), the worse the localization accuracy would be (the worst localization accuracy is around $0.2\,\text{mm}$ at $x = 3\,\text{mm}$). This is because the tangent function $\tan(kX)$ becomes steeper as X increases, and therefore a small fluctuation of X would lead to a large variation of $\tan(kX)$ (or R_B value) especially when X is close to the half period of $\tan(kX)$.

Fig. 3(b) shows the mean values of X_1 and X_2 under different sphere diameters and elastomer thickness. It is found that the thicker the elastomer layer is (or the smaller the sphere diameter is), the larger the X mean value (thus the worse the localization accuracy) would be (see Fig. 3(a)). The same conclusion can be drawn from Fig. 3(c), where the period of the R_B mean curve increases as the elastomer thickness decreases or the diameter of the contact object increases, and a larger period of the R_B mean curve corresponds to a better localization accuracy (Fig. 3(a)).

In summary, the proposed super-resolution model gives the relationship between the R_B mean curve and contact location

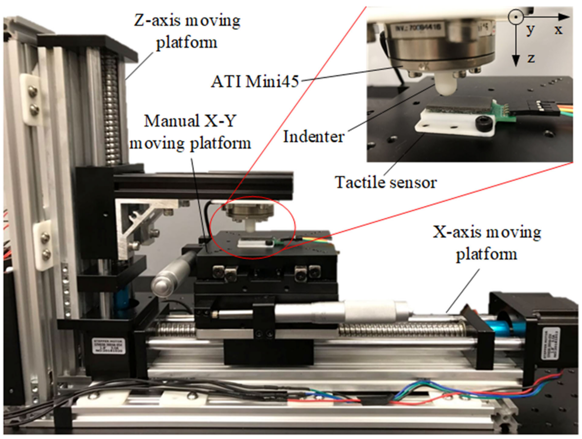

Fig. 4. The overall experimental setup.

x, and given the R_B value (i.e., B_x/B_z) measured by the Hall sensor, the corresponding contact location x can be estimated by looking up Fig. 3(a) (i.e., $x = (1/k)arctan(R_B)$). Since the R_B mean curve is weakly coupled with the contact force (reflected by R_B range), the model's localization accuracy is determined by the minimum interval of contact locations whose R_B ranges do not overlap each other. We observe that the length (or size) of the R_B ranges are proportional to the period of the R_B mean curve, and it can be adjusted by designing the period of the flexible magnetic film ((4) and Fig. 3(a)) and the thickness of the elastomer layer (Fig. 3(c)). Once we obtain the contact location, the corresponding contact force can be estimated by looking up Fig. 5, and the details of the force estimation will be introduced in Section V-C.

V. Experimental Results

A. Data Collection

The experimental setup for data collection is shown in Fig. 4, which consists of two motor-driven moving platforms (along X-axis and Z-axis, respectively) and a 2-axis manual moving platform (along X-axis and Y-axis, respectively). The tactile sensor was fixed on the manual X-Y platform, and a 6-axis F/T sensor (ATI Mini-45) with a 3D-printed indenter fixed on it was mounted on the Z-axis motor-driven platform to monitor the force applied on the tactile sensor.

During data collection, a semi-spherical indenter of $20\,\mathrm{mm}$ diameter was pressed on the tactile sensor ($18\,\mathrm{mm}$ in length) with an interval of $0.2\,\mathrm{mm}$ along both x and z directions, generating 91 contact points along x direction (from 0 to $18\,\mathrm{mm}$) and five indentation levels (from $0.2\,\mathrm{mm}$ to $1\,\mathrm{mm}$) along z direction, respectively. Data from the tactile sensor were collected with the Arduino Mega 2560 via the I^2C protocol, and the data from ATI Mini45 were acquired with Python via TCP/IP protocol.

B. Estimation of Contact Location

Based on the working principle of the tactile sensor (Fig. 1(b)), we can roughly locate the contact force to the left ($B_x > 0$) or right ($B_x < 0$) side of the Hall sensor that has the largest B_z among the three sensors. This has been verified by the experimental measurements of the sensor response (also see our previous work [12]). As shown in Fig. 5(a), the B_x and B_z readings when the sensor was pressed from 0 to $18\,\mathrm{mm}$ at a particular indentation depth ($\Delta z = 1\,\mathrm{mm}$) are put together. It is found that the Hall sensor nearest to the contact location has the largest B_z reading, and the B_x reading of the Hall sensor has opposite signs if the contact force is applied on different sides of the sensor. Therefore, we can first locate the contact force to one of the three Hall sensors (e.g., S_2) that is activated most or has the largest B_z reading, and then we can further target the contact location to the right side of S_2 if $B_{x2} > 0$. For estimating the accurate contact location, an experimental R_B curve should be given for the proposed super-resolution model.

Assume the expression of B_x and B_z curves in Fig. 5(a) are:

$$B_x = a_1(z)\sin(kx), \quad B_z = a_2(z)\cos(kx) \tag{8}$$

where $a_1(z)$ and $a_2(z)$ indicate the amplitudes related with indentation depth Δz, and k is the wavenumber which equals $2\pi/T_1$ where T_1 is the period of the sine and cosine function, then the ratio of B_x and B_z would be:

$$R_B = \frac{B_x}{B_z} = a(z)\tan(kx), \tag{9}$$

where $a(z) = a_1(z)/a_2(z)$, $k = \pi/T_2$, and T_2 is the period of $\tan(kx)$.

Taking the area S_{2R} (the right side of Hall sensor S_2) as an example, the R_B mean curve is obtained by calculating the mean values of the ratio of B_x and B_z under 5 levels of indentation depth (from $\Delta z = 0.2\,\mathrm{mm}$ to $\Delta z = 1\,\mathrm{mm}$) and then fitting them by (9). The fitting curve of the R_B mean values (referred to as R_B mean curve) and the R_B range defined by the minimum and maximum R_B values at each x location are shown in Fig. 5(b). We observe that the values of R_B range increase when the pressing location x increases, while R_B ranges almost have no overlap at different x locations, which is consistent with the theoretical result (Fig. 3(a)). With this experimental R_B mean curve, we look up the precise contact location x using the R_B value calculated with the measurements of B_x and B_z from the sensor (i.e., $x = (1/k)arctan(R_B/a(z))$. For example, if R_B is 0.46, then the corresponding contact location x would be $1.6\,\mathrm{mm}$.

We note that when the contact location is remote from Hall sensor's center (e.g., in the middle of two neighboring Hall sensors), the indentation depth should be no less than $0.2\,\mathrm{mm}$ so that the deformation of the magnetic film is large enough to be captured by the Hall sensors. Moreover, since no overlapping signals of neighboring taxels are required for the proposed super-resolution model, the above method can be adapted to to detect multipoint contact by setting an activation threshold of B_z readings for each taxel (rather than comparing B_z among all taxels). For example, an increase threshold of $100\,\mathrm{uT}$ for the B_z readings of all three Hall sensors is set to detect multi touch in Supplementary video 1.

C. Estimation of Force Magnitude

Based on (9) and results in Fig. 5(b), we have shown that the R_B value at a particular pressing location x is insensitive to the

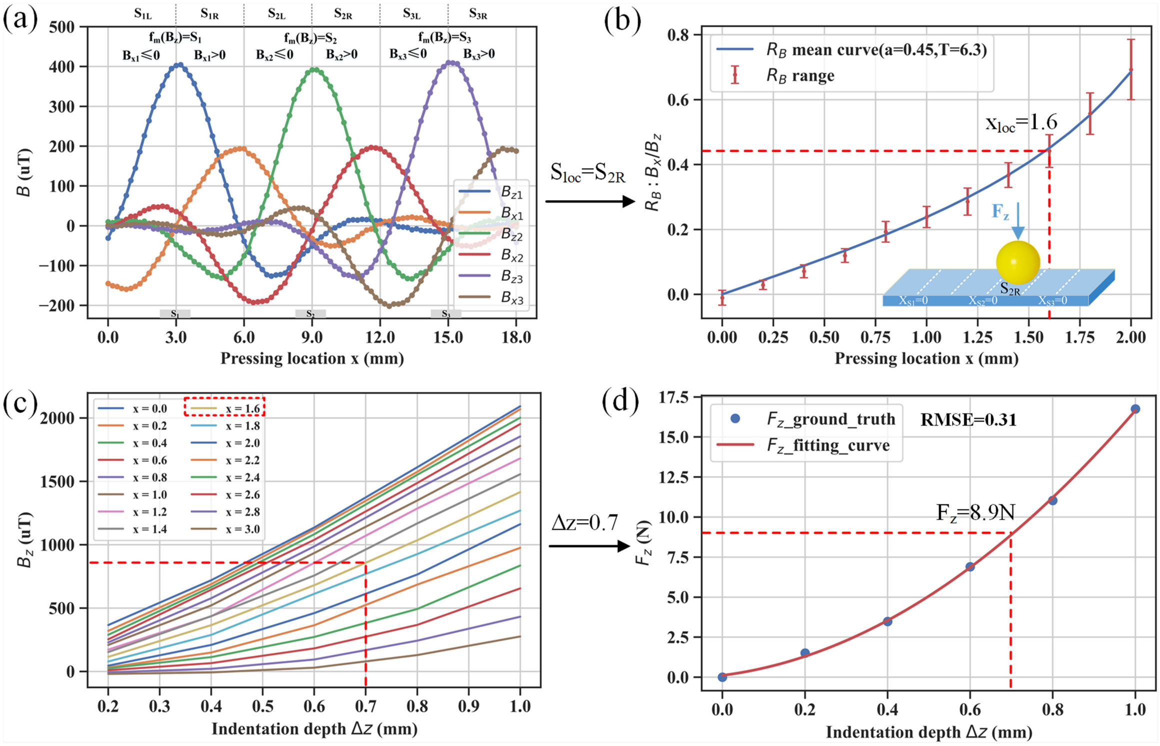

Fig. 5. Flowchart of the proposed super-resolution method. (a) Coarse localization: locate the applied normal force F_z into one of the six subareas of the tactile sensor by comparing the B_x and B_z values (for example, $S_{loc} = S_{2R}$ here). (b) Fine localization: accurately estimate the contact location within the subarea S_{2R} according to the R_B value (for example, $x_{loc} = 1.6\,\mathrm{mm}$ here). (c) Intermediate step: estimate the indentation depth Δz according to the B_{z2} and x_{loc} (for example, $\Delta z = 0.7\,\mathrm{mm}$ here). (d) Force estimation: estimate the force magnitude F_z according to the Δz (for example, $F_z = 8.9\,\mathrm{N}$ here).

change of the indentation depth Δz, which allows us to precisely locate a normal force from the R_B mean curve. However, the individual reading of B_x or B_z at a particular pressing location is highly associated with the indentation depth. By taking the subarea S_{2R} as an example, Fig. 5(c) shows the B_z curves under different indentation depths at different pressing locations, from which we inversely look up the indentation depth Δz according to the current B_z reading from sensor and the pressing location x estimated from the R_B mean curve (Fig. 5(b)). For example, if the B_z reading is $858\,\mathrm{uT}$ and the contact location $x = 1.6\,\mathrm{mm}$, the corresponding pressing depth Δz would be $0.7\,\mathrm{mm}$ in Fig. 5(c).

Once we obtain the indentation depth Δz, the corresponding force magnitude F_z can be calculated using the force fitting curve as shown in Fig. 5(d) (with RMSE of $0.31\,\mathrm{N}$), where F_z is proportional to the indentation depth. For example, if the indentation depth Δz is $0.7\,\mathrm{mm}$, then the corresponding force magnitude F_z would be $8.9\,\mathrm{N}$.

Fig. 5(c) and Fig. 5(d) can be regarded as two lookup tables. We can obtain the indentation depth Δz from the first lookup table and then find the corresponding force magnitude F_z in the second one. These two tables are generated using a calibration indenter of $20\,\mathrm{mm}$ diameter, and the data are collected at an interval of $0.2\,\mathrm{mm}$ for both the contact location x and indentation depth Δz. To fill in missing data, linear interpolation is applied, and for objects with different diameters, the lookup tables should be calibrated individually.

D. R_B Mean Curve Under Different Conditions

The key concept of the proposed super-resolution model is the R_B mean curve, from which we can obtain the contact location according to the R_B value. To investigate how the elastomer thickness and object diameter would influence the properties of the R_B mean curve, we built three tactile sensors of different elastomer thicknesses and calibrated them using four indenters of different diameters as shown in Fig. 6(a).

Again, taking the subarea S_{2R} as an example whose local Y-axis is at $x = 9\,\mathrm{mm}$, we use (9) to fit the R_B mean curves for all combinations of elastomer thicknesses and indenter diameters. The fitting curves are shown in Fig. 6(a)–(c) (with parameters listed in Table I), where the sharp increase of each curve indicates the pressing location is close to the half period ($T/2$) of the R_B mean curve (or the tangent function).

We observe that the R_B values close to the half period location change dramatically even with a small variation of the pressing location, and this is not beneficial to stably estimate the contact location near the half period areas. Therefore, it is preferable to design a tactile sensor whose half period of R_B mean curve lies out of the sub-sensing area, for example, as the one shown in Fig. 6(a), where the half period of R_B mean curve are mostly larger than the length of the sub-sensing area (i.e., half period of the flexible magnetic film) – $3\,\mathrm{mm}$.

As Fig. 6(e) shows, the half period of R_B mean curves tend to increase as the elastomer thickness decreases and the indenters diameter increases, which is consistent with the theoretical

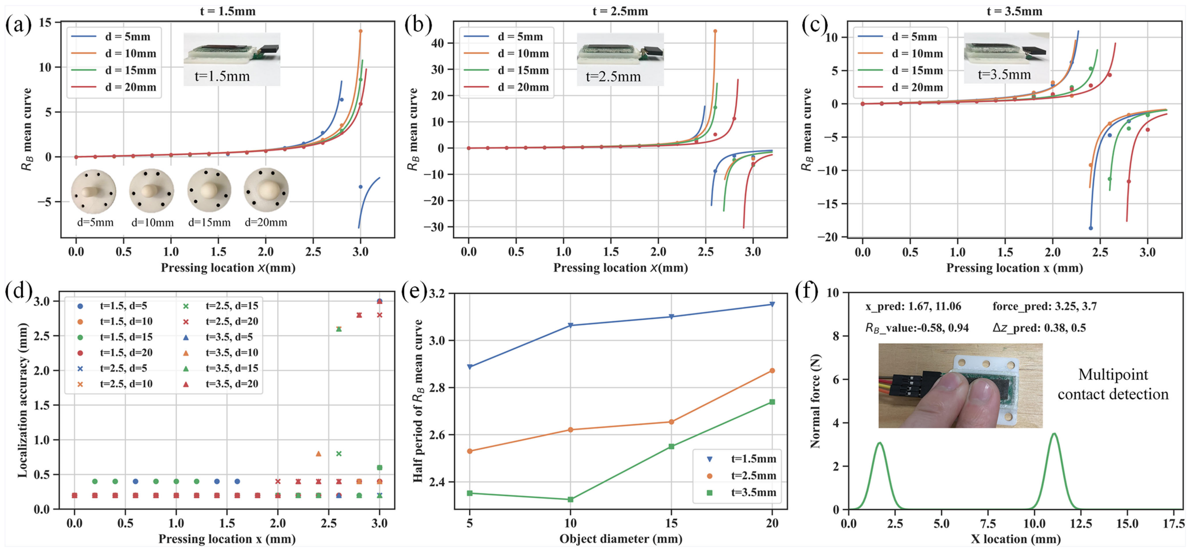

Fig. 6. (a)-(c) R_B mean curves under different indenter diameters when the elastomer thickness t is 1.5 mm, 2.5 mm, and 3.5 mm respectively. (d) Localization accuracy at different contact position x. (e) Half period $T/2$ of R_B mean curves under different indenter diameters and elastomer thicknesses. (f) Estimation of contact location and force magnitude of multipoint contact (here, the Gaussian distribution is just for showing the contact location and force magnitude predicted by the model, rather than the real distribution of the contact force).

TABLE I
FITTING PARAMETERS OF THE R_B MEAN CURVE AND LOCALIZATION ACCURACY UNDER DIFFERENT CONDITIONS

Elastomer thickness t (mm)		1.5				2.5				3.5			
Indenter diameter d (mm)		5	10	15	20	5	10	15	20	5	10	15	20
Fitting parameters of R_B mean curve	a	0.4	0.46	0.44	0.45	0.4	0.56	0.5	0.46	0.6	0.55	0.4	0.5
	$T/2$	2.89	3.06	3.10	3.15	2.53	2.62	2.65	2.87	2.35	2.32	2.55	2.74
Percentage of valid length ($L_V/3 \times 100\%$)		0.93	0.99	1	1	0.81	0.84	0.85	0.92	0.75	0.74	0.82	0.88
Mean absolute error within L_v (mm)		0.28	0.24	0.27	0.21	0.2	0.2	0.2	0.25	0.2	0.22	0.2	0.22
Worst localization accuracy within L_v (mm)		0.4	0.4	0.4	0.4	0.2	0.2	0.2	0.4	0.2	0.4	0.2	0.4
Best localization accuracy (mm)		0.2											

results in Fig. 3(c). Thus, to increase the half period of R_B mean curve, we design a thin elastomer layer while still ensuring sufficient room for the sensor deformation. Here we chose the thickness 1.5 mm. We note that reducing elastomer layer thickness is not the only way to increase the half period of the R_B mean curve. Adjusting other parameters at the very beginning of sensor designing stage could also change the properties of the R_B mean curve, such as magnetic sensor layout, the flexible magnet's period and thickness.

The localization accuracy at different contact location is shown in Fig. 6(d). It is found that the localization accuracy is less than 0.4 mm when the contact location (relative to the center of the Hall sensor) is smaller than 2.4 mm while it becomes worse when the contact location approaches the half period of R_B mean curve, which indicates that localization accuracy is highly associated with the half period of the R_B mean curve and it is necessary to increase the half period $T/2$ by properly designing the tactile sensor in practice.

As the localization accuracy near the half period of R_B mean curve is poor, we define tactile sensor's valid length as:

$$L_v = T/2 - 0.1. \tag{10}$$

The percentage of the valid length relative to the full sensing length of a subarea (3 mm) and the localization accuracy within the valid length are listed in Table I. It is found that the percentage of the valid length for 1.5 mm thickness tactile sensor is the largest, which is close to its full sensing length. Moreover, the localization errors within the valid length of all tactile sensors are no more than 0.3 mm on average and 0.4 mm in the worst case, indicating that a 15-fold improvement of the localization accuracy (from 6 mm to 0.4 mm) has been achieved for our tactile sensor.

Finally, we evaluated the performance of our model on unseen (or uncalibrated) objects of different shapes and sizes, with the assumption that objects of non-spherical shape can be regarded as a sphere of an equivalent diameter such that the sphere can evoke the same sensor responses as the non-spherical object. As shown in Fig. 6(f), we estimate the force locations and magnitude of a multipoint contact made by human fingers, and both fingers are successfully detected by using the proposed model (calibrated with a spherical indenter of 20 mm diameter on the sensor of 2.5 mm elastomer thickness). However, both the estimated values of force location and magnitude would be slightly larger than the actual ones (see Fig. 3 and Fig. 6) since the equivalent diameter of human fingers (~15 mm) is smaller than that of the calibration sphere (20 mm). Using the same sensor and model, we demonstrate the online estimation of force location and magnitude for unseen objects as shown in the supplementary video. It shows that the proposed model can still work well on unseen objects but with a drop in performance, since the equivalent diameter of those unseen objects is either smaller or larger than that of the calibration sphere ($20\,\mathrm{mm}$). Given that the half period of R_B mean curve is almost linearly correlated with the object diameter (Fig. 3(c)), a compensation coefficient could be learned and added to the pre-calibrated model so that it can adapt to different contact shapes and sizes without recalibration.

VI. Discussion and Future Work

By using the proposed tactile super-resolution method, we have attained a 15-fold improvement of localization accuracy and the capability of measuring the magnitude of the contact force. More importantly, such performance is achieved by using just a single 3-axis taxel since no overlapping signals are required for the proposed super-resolution model. This ensures that the proposed model can work properly even when the neighbouring taxels of the most activated one (nearest to the contact position) are damaged or unavailable.

We observe that the localization accuracy of the sensor mainly depends on the half period ($T/2$) of the R_B mean curve, and to achieve the best localization accuracy, the half period should be larger than the length of subareas ($3\,\mathrm{mm}$ in our setup), which is half of the distance between two neighboring magnetic sensors. In addition, both theoretical and experimental results show that for a given flexible magnetic film, the half period of the R_B mean curve is proportional to the object diameter and inversely proportional to the thickness of the elastomer layer, which provides insight into tactile sensor design for particular applications.

However, the theoretical R_B $(\tan(kX))$ values (Fig. 3(a)) is actually smaller than the experimental ones at the same contact location (Fig. 5(b)). In addition, the theoretical values of the half period of the R_B mean curve (Fig. 3(c)) are much larger than the experimental ones (Fig. 6(e)) although the variation trends of the half period under different indenter diameters and elastomer thicknesses are the same. This is because the real case is not as ideal as described in the assumptions of the model, and the fabrication of the sensor could also introduce some unseen defects that affect the experimental results.

In real cases, the magnetic properties of the flexible magnet would be slightly changed due to the compression of the magnet under pressure. And except for the rotation, there would be more complex redistribution (e.g., superposition) of the magnetic field when the flexible magnet deforms, and such magnetic redistribution is not considered in the model. To precisely describe and estimate the behavior of deformed Halbach magnets, a finite element model (FEM) could be developed in the future. With the FEM model, we can collect a large dataset of sensor deformation fields generated by arbitrary contact shapes (spherical and non-spherical) and three-dimensional forces (normal and non-normal) from simulation. Then we can train a generic super-resolution model that covers various contact conditions in the simulator and then transfer it to the real world. We will investigate the effectiveness of the sim-to-real transfer method on the planned generic model.

References

[1] Z. Kappassov, J.-A. Corrales, and V. Perdereau, "Tactile sensing in dexterous robot hands," *Robot. Auton. Syst.*, vol. 74, pp. 195–220, 2015.

[2] L. Zou, C. Ge, Z. Wang, E. Cretu, and X. Li, "Novel tactile sensor technology and smart tactile sensing systems: A review," *Sensors*, vol. 17, no. 11, p. 2653, 2017.

[3] F. Xu *et al.*, "Recent developments for flexible pressure sensors: A review," *Micromachines*, vol. 9, no. 11, p. 580, 2018.

[4] Q. Li, O. Kroemer, Z. Su, F. F. Veiga, M. Kaboli, and H. J. Ritter, "A review of tactile information: Perception and action through touch," *IEEE Trans. Robot.*, vol. 36, no. 6, pp. 1619–1634, Dec. 2020.

[5] G. Pang, G. Yang, and Z. Pang, "Review of robot skin: A potential enabler for safe collaboration, immersive teleoperation, and affective interaction of future collaborative robots," *IEEE Trans. Med. Robot. Bionics*, vol. 3, no. 3, pp. 681–700, Aug. 2021.

[6] M. R. Cutkosky, R. D. Howe, and W. R. Provancher, "Force and tactile sensors," in *Springer Handbook of Robotics*, B. Siciliano and O. Khatib, Eds. Berlin, Heidelberg, Germany: Springer, pp. 455–476, 2008.

[7] S. Sundaram, P. Kellnhofer, Y. Li, J.-Y. Zhu, A. Torralba, and W. Matusik, "Learning the signatures of the human grasp using a scalable tactile glove," *Nature*, vol. 569, no. 7758, pp. 698–702, 2019.

[8] V. E. Abraira and D. D. Ginty, "The sensory neurons of touch," *Neuron*, vol. 79, no. 4, pp. 618–639, 2013.

[9] W. Yuan, S. Dong, and E. H. Adelson, "Gelsight: High-resolution robot tactile sensors for estimating geometry and force," *Sensors*, vol. 17, no. 12, p. 2762, 2017.

[10] E. Donlon, S. Dong, M. Liu, J. Li, E. Adelson, and A. Rodriguez, "Gelslim: A high-resolution, compact, robust, and calibrated tactile-sensing finger," in *Proc. IEEE/RSJ Int. Conf. Intell. Robots Syst*., 2018, pp. 1927–1934.

[11] J. M. Loomis, "An investigation of tactile hyperacuity," *Sensory Processes*, vol. 3, no. 4, pp. 289–302, 1979.

[12] Y. Yan *et al.*, "Soft magnetic skin for super-resolution tactile sensing with force self-decoupling," *Sci. Robot.*, vol. 6, no. 51, 2021, Art. no. eabc8801.

[13] J. Mallinson, "One-sided fluxes–A magnetic curiosity?," *IEEE Trans. Magn.*, vol. 9, no. 4, pp. 678–682, Dec. 1973.

[14] N. F. Lepora, U. Martinez-Hernandez, M. Evans, L. Natale, G. Metta, and T. J. Prescott, "Tactile superresolution and biomimetic hyperacuity," *IEEE Trans. Robot.*, vol. 31, no. 3, pp. 605–618, Jun. 2015.

[15] N. F. Lepora and B. Ward-Cherrier, "Superresolution with an optical tactile sensor," in *Proc. IEEE/RSJ Int. Conf. Intell. Robots Syst*., 2015, pp. 2686–2691.

[16] B. Ward-Cherrier *et al.*, "The tactip family: Soft optical tactile sensors with 3D-printed biomimetic morphologies," *Soft Robot.*, vol. 5, no. 2, pp. 216–227, 2018.

[17] P. Piacenza, S. Sherman, and M. Ciocarlie, "Data-driven super-resolution on a tactile dome," *IEEE Robot. Autom. Lett.*, vol. 3, no. 3, pp. 1434–1441, Jul. 2018.

[18] T. Hellebrekers, N. Chang, K. Chin, M. J. Ford, O. Kroemer, and C. Majidi, "Soft magnetic tactile skin for continuous force and location estimation using neural networks," *IEEE Robot. Autom. Lett.*, vol. 5, no. 3, pp. 3892–3898, Jul. 2020.

[19] R. Bhirangi, T. Hellebrekers, C. Majidi, and A. Gupta, "Reskin: Versatile, replaceable, lasting tactile skins," 2021, *arXiv:2111.00071*.

[20] P. Piacenza, K. Behrman, B. Schifferer, I. Kymissis, and M. Ciocarlie, "A sensorized multicurved robot finger with data-driven touch sensing via overlapping light signals," *IEEE/ASME Trans. Mechatronics.*, vol. 25, no. 5, pp. 2416–2427, Feb. 2020.

[21] H. Sun and G. Martius, "Machine learning for haptics: Inferring multi-contact stimulation from sparse sensor configuration," *Front. Neurorobot.*, vol. 13, p. 51, 2019.

[22] M. Kim, H. Choi, K.-J. Cho, and S. Jo, "Single to multi: Data-driven high resolution calibration method for piezoresistive sensor array," *IEEE Robot. Autom. Lett.*, vol. 6, no. 3, pp. 4970–4977, Jul. 2021.

[23] H. Sun and G. Martius, "Theory of geometric super-resolution for haptic sensor design," 2021, *arXiv:2105.11914*.

[24] Y. Yan and J. Pan, "Fast localization and segmentation of tissue abnormalities by autonomous robotic palpation," *IEEE Robot. Autom. Lett.*, vol. 6, no. 2, pp. 1707–1714, Apr. 2021.

[25] Y. Yan, Z. Hu, Y. Shen, and J. Pan, "Surface texture recognition by deep learning-enhanced tactile sensing," *Adv. Intell. Syst.*, 2021, Art. no. 2100076.